

Terahertz Scanless Hypertemporal Imaging

Luca Zanotto, Giacomo Balistreri, Andrea Rovere, O-Pil Kwon, Roberto Morandotti, Riccardo Piccoli,* and Luca Razzari*

Since its first demonstration in 1995, terahertz time-domain imaging has attracted an increasingly growing interest for its ability to reveal spectral fingerprints of materials and probe changes in refractive index and absorption, as well as detect the inner structure of complex objects via time-of-flight measurements. Practically, however, its widespread use has been hampered by the very long acquisition time typically required to spatially raster-scan the object, and for each spatial point, record the field in time via a delay line. Here, this fundamental bottleneck is addressed by implementing a scanless single-pixel imaging scheme, which sets the path for an unprecedented reduction of both system complexity and acquisition time. By properly exploiting natural wave diffraction, time-to-space encoding applied to terahertz point detection allows for an almost instantaneous capture of the terahertz waveforms, while multidimensional images are reconstructed via a computational approach. The scheme is a promising solution for the development of next-generation fast and compact terahertz imagers perfectly suitable for high-repetition-rate laser sources.

through many optically-opaque materials (e.g., plastics, semiconductors, papers),^[1] allowing for the exposure of concealed objects^[2] or the study of layered structures,^[3] as well as a low photon energy (meV), which makes it intrinsically safe to use. In particular, time-domain spectroscopy (TDS), arguably the most powerful THz experimental technique, enables the coherent detection (i.e., the retrieval of both amplitude and phase) of the electric field associated with THz pulses.^[4] As a result, it allows for the full characterization of the optical properties of an arbitrary material (e.g., the complex refractive index),^[5] as well as the probing of rotational/vibrational transitions or collective excitations, such as phonons, characteristic of a variety of substances at THz frequencies (e.g., gases,^[6] liquids,^[7] organic/inorganic materials,^[8,9] bio-

molecules^[10]). Moreover, the picosecond duration of THz pulses enables their use to perform time-resolved measurements of certain phenomena occurring on very short time scales,^[11] or even to uniquely drive and control certain others.^[12] The extension of these capabilities to imaging^[13] is thus a very promising technology for a large variety of purposes, including security,^[14] quality and safety control in industry,^[2,15] biomedical applications,^[16,17] and also art conservation.^[18,19]

In contrast to popular detection techniques based on photo-/thermo-electric effects, a number of novel approaches have been developed to directly retrieve the electric field associated with a THz pulse. However, this often requires sampling the THz waveform with a shorter and variably delayed optical gating pulse,^[20–22] which makes the acquisition process rather slow and cumbersome. Additionally, for imaging applications, the object typically has to be also raster-scanned pixel-by-pixel, thus rendering the technique complex to implement beyond research settings.^[23] To address both issues and pave the way for THz hypertemporal imaging in real time, we propose a scheme that combines the single-pixel imaging (SPI) method in space, to avoid raster-scanning the object, and a scanless detection technique in time, to avoid the temporal reconstruction of the THz waveform by means of a delay line (see simplified schematic in **Figure 1**).


1. Introduction

During the last 30 years, terahertz (THz) technologies have experienced a steady growth and today are recognized as powerful tools for interrogating materials, since they provide information complementary to that obtained using microwaves, infrared/visible/ultraviolet (IR/VIS/UV) light, and X-rays. THz radiation has some unique features, such as the ability to pass

L. Zanotto, G. Balistreri, A. Rovere, R. Morandotti, R. Piccoli, L. Razzari
Institut National de la Recherche Scientifique
Centre Énergie Matériaux Télécommunications (INRS-EMT)
Varenes, Quebec J3X 1P7, Canada
E-mail: riccardo.piccoli@polimi.it; luca.razzari@inrs.ca

O-P. Kwon
Department of Molecular Science and Technology
Ajou University
Suwon 443–749, South Korea

R. Piccoli
Department of Physics, Piazza Leonardo Da Vinci
Politecnico di Milano
Milano 32, I-20133, Italy

 The ORCID identification number(s) for the author(s) of this article can be found under <https://doi.org/10.1002/lpor.202200936>

© 2023 The Authors. Laser & Photonics Reviews published by Wiley-VCH GmbH. This is an open access article under the terms of the Creative Commons Attribution-NonCommercial-NoDerivs License, which permits use and distribution in any medium, provided the original work is properly cited, the use is non-commercial and no modifications or adaptations are made.

DOI: 10.1002/lpor.202200936

2. Single-Pixel Imaging, Diffraction, and THz Scanless Detection

SPI was first demonstrated in the work “Dual photography” by Sen et al.^[24] in 2005, and has fostered a great deal of research

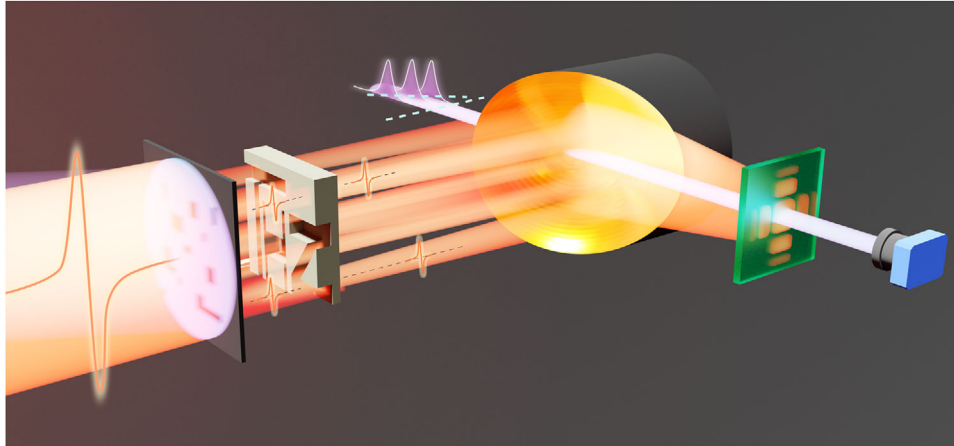


Figure 1. Illustration of the scanless-SPI technique. The incoming THz pulse (in orange from left) is first spatially modulated, then propagates through the semitransparent sample (“THz” shape), and eventually reaches the detection crystal after being focused by an off-axis parabolic mirror. The probe pulse (featuring a tilted front) samples the center of the spatial Fourier transform of the THz wave distribution in the focal plane of the parabolic mirror, where the probe optical sampling detector is placed (green crystal on the right). The probe spatial intensity is finally recorded by a camera (blue device on the right).

ever since. SPI enables the reconstruction of an image using a detector without spatial resolution, by measuring the correlation between a set of light patterns and the spatial features of the object under investigation. Such correlation is evaluated by simply recording the transmitted (or reflected) light with the single-pixel detector. A reconstruction algorithm subsequently enables the retrieval of the original image. Duarte et al.^[25] identified SPI as a suitable technique to implement the concept of compressed sensing (CS) for imaging purposes. CS describes the conditions under which it is possible to reconstruct a signal from an under-sampled dataset.^[26] The compressibility of an image is related to the concept of “sparsity,” which directly connects to the number of non-zero entries in the vector representing the image. The implementation of CS in SPI-based systems makes it possible to significantly boost the speed performance when detector arrays are unavailable or very expensive.^[27] One such case is that of THz radiation, which is the reason why THz SPI has become a widely explored solution, starting from its first demonstration in 2008.^[28] In the subsequent years, numerous studies led to improvements in the modulation technique employed to create the THz patterns, for example by using a spinning disk,^[29] a photo-excited semiconductor,^[30] or active metamaterials.^[31] While these works made the use of SPI at THz frequencies progressively more efficient, they all either retrieved only the amplitude of the THz field at a specific time position, or relied on a sequential scan of the time domain, typically performed with a mechanical delay line, to obtain the THz temporal waveform. The same is also true for other works that proved the effectiveness of SPI in typical situations where THz imaging is applied, such as spectral imaging,^[32] near-field imaging,^[33] and time-of-flight imaging.^[34] A comprehensive review of these investigations can be found in ref. [35]. Differently from all these studies, our system enables the simultaneous capture of the whole THz temporal waveform, in addition to the retrieval of the object spatial profile via SPI, as will be discussed in the following.

It is instructive to connect the mechanism underlying SPI and the wave nature of light. The well-known Huygens-Fresnel prin-

ciple elegantly catches the physics behind diffraction.^[36] According to this principle, the complex field amplitude in a single point after free-space propagation can be interpreted as a summation of all the spherical waves generated at every point of the source plane (see Supporting Information). Therefore, even though one might believe that diffraction is a detrimental effect that befores image reconstruction, we show here how the correct operation of our scheme strictly relies on its existence. As mentioned earlier, thanks to the structured illumination characteristic of SPI, we only need a measurement of the correlation between patterns and the object’s spatial shape. Diffraction automatically performs the spatial integration that brings the correlation information to a single point, thus naturally delivering the working conditions for SPI. We can see how this occurs by putting the problem in mathematical terms. The diffraction solution for a propagating patterned beam can be reduced to a spatial integral of the product between the n th pattern distribution, $P_n(\xi, \eta)$, and the transmission (reflection) function of the object, $T(\xi, \eta)$:

$$W_n \propto \iint_{\Sigma} P_n(\xi, \eta) T(\xi, \eta) d\xi d\eta \quad (1)$$

where (ξ, η) are the spatial coordinates, while Σ is the relevant area at the input plane. W_n is the point value of the electric field at the center of the observation plane and corresponds to the quantity recorded by the single-pixel detector for the n th pattern (see Supporting Information for a detailed mathematical derivation). The integral in Equation (1) gives a measure of the correlation between $P_n(\xi, \eta)$ and $T(\xi, \eta)$, being therefore mathematically equivalent to an SPI problem. In principle, then, simple free-space propagation suffices to perform an SPI measurement, yet, typically, a focusing element is employed to concentrate the energy and improve the related signal-to-noise ratio (SNR) (see Supporting Information). In addition, since at THz frequencies coherent detection directly enables the retrieval of the complex value of the electric field at the detection point, complete (i.e.,

amplitude and phase) image reconstruction can be achieved, even in the most general case where all the entities involved (i.e., patterns and object transmission/reflection) are complex-valued. The phenomenon of diffraction has been exploited in various SPI-based arrangements operating in the VIS/IR range, like in systems for lens-free diffractive imaging,^[37] as well as in setups for complex field retrieval utilizing ptychography^[38] and digital holography.^[39]

In our imaging system, a scanless THz detection technique (also typically referred to as “single-shot,” for its ability to potentially operate with an individual pulse) has been judiciously coupled to SPI by means of diffraction, to address the issue of the slow and complex point-by-point temporal scan needed to obtain the THz waveform. Indeed, while an SPI-based THz imaging system has recently reached real-time operation for fixed time amplitude measurements,^[40] the full potential of THz time-domain imaging in practical implementations is still untapped, due to the limits imposed by the temporal scan. Traditionally, this scan is performed via a mechanical delay line, which varies the delay of a probe pulse relative to the THz wave. Such delay lines are based on mechanical moving parts that are prone to failure and significantly slow down the acquisition process. All-optical^[41] and acousto-optical^[42] delay lines with sampling rates up to hundreds of Hz and tens of kHz, respectively, have been recently developed. These systems enable fast operation without moving parts, yet they require the use of two accurately synchronized lasers in the first case, or a dedicated acousto-optical modulator and sophisticated electronics in the second, which considerably increase the complexity and cost of the imaging system. During the last 20 years, single-shot techniques have been explored as tools to simultaneously record the whole THz waveform in the time-domain. They are generally based on stretching the probe pulse temporally or spreading it spatially, thus allowing different temporal positions of the waveform to be probed at once.^[43] In particular, time-to-space mapping relies on tilting the probe pulse front so that spatially separated points arrive at the detector plane at different times, therefore probing different temporal portions of the THz pulse.^[44] Thereafter, the probe spatial intensity is captured with a camera, obtaining an in principle instantaneous picture of the THz temporal waveform. At a first glance, combining SPI and such time-to-space encoding technique may seem impracticable. Indeed, it would be reasonable to think that, by using a spatial coordinate to allocate the time domain, the former would be no longer accessible for the retrieval of the 2D image of the object. In this work, we demonstrate that this is instead possible, thanks to the large wavelength mismatch between the THz and IR probe beams. In this regard, once again diffraction represents a key aspect. To achieve a “true” “single-point” detection^[45] and satisfy the conditions under which Equation (1) is valid, the probe size at the detector plane should be smaller than the width w of the main lobe of the THz diffracted pattern at the same plane (for pure free-space propagation, $w = \lambda_{\text{THz}}z/x_{\text{MAX}}$, where λ_{THz} is the THz wavelength, z the propagation distance, and x_{MAX} the scene maximum spatial extent;^[36] in our specific experimental configuration, w is estimated to be ≈ 1.5 mm, see Supporting Information). This is reasonably simple to achieve using a probe beam at IR/VIS wavelengths, almost three orders of magnitude shorter than that of THz radiation. By keeping the probe smaller than this size, in a somehow counter-intuitive fashion, we can

exploit the transverse spatial dimension of the probe beam to allocate the time domain, while still being able to effectively probe a “single point” of the THz field spatial distribution at the detector plane, which is the necessary condition for SPI. In this way, we can obtain a complete spatiotemporal reconstruction of the object to be imaged, at the same time avoiding the strict limitations in temporal resolution that would be imposed by a time-to-frequency encoding strategy.^[46] Such innovation makes it possible to realize a THz hypertemporal imaging system with no moving parts, thus being faster, more robust, and compact than standard implementations.

2.1. Experimental Setup and Testbed Samples

Our experimental setup is illustrated in **Figure 2a**. A third line is added to the two employed for THz generation and probing, where a fraction of the laser beam is spatially patterned by means of a Digital Micromirror Device (DMD; see Experimental Section) and then used for THz photo-modulation.^[30] In the probe beamline, a diffraction grating is used to tilt the probe pulse front. Such tilted probe is then imaged onto the electro-optic detection crystal, to enable the capture of the THz waveform in the time-domain, and finally propagates to reach the IR camera (see Experimental Section). This eliminates the need for the temporal scan typically performed with a delay line. In **Figure 2b**, we can see examples of probe images recorded by the IR camera. The THz waveform is extracted by subtracting the background probe image from the one modulated by the THz beam. A proper normalization is also performed, to correct for the probe intensity profile (see Experimental Section). In **Figure 2c**, we show an example of the portion of the processed camera image used for the temporal trace retrieval, as well as the actual THz waveform obtained by integrating along the vertical direction to improve the SNR.

THz image reconstruction is achieved by means of a time-domain SPI algorithm (see ref. [34] for further details), implemented by solving a system of n equations for each point in time t_i : $W_n(t_i) = \sum_{x,y} P_n(x,y)T(x,y,t_i)$, where $T(x,y,t_i)$ is the transmission function of the sample (i.e., the image to be retrieved), $W_n(t_i)$ is the n th-detector’s reading and $P_n(x,y)$ the n th-pattern used to illuminate the sample. This procedure takes the THz waveforms $W_n(t)$ captured for each pattern $P_n(x,y)$ and yields the THz waveforms $T(x_j,y_k,t)$ corresponding to each pixel of the image (x_j,y_k) . The output is thus a spatiotemporal data cube that contains the exact same information that would be acquired with a traditional (scan-based) TDS imaging system.

To prove the potential of the proposed imaging scheme, in what follows we show the reconstruction of 3D images of multilayered samples, by displaying the layer contrast with different methods. We employed two samples made of high-density polyethylene (HDPE), which has a refractive index of 1.54 and negligible absorption ($\alpha \leq 1 \text{ cm}^{-1}$) in the range 0.5–2.5 THz.^[47] Sample (1) (**Figure 3a**) has the letters T-H-Z engraved with different thicknesses ($T = 1$ mm, H and $Z = 2$ mm, outside area = 3 mm), while sample (2) (**Figure 3b**) has the letters I-N-R-S engraved (I and N —in air, R and $S = 1$ mm, outside area = 2 mm).

2.2. THz Field Amplitude Images

We first reconstructed images while considering the THz field amplitude at various time positions. In **Figure 3c,d** we show three

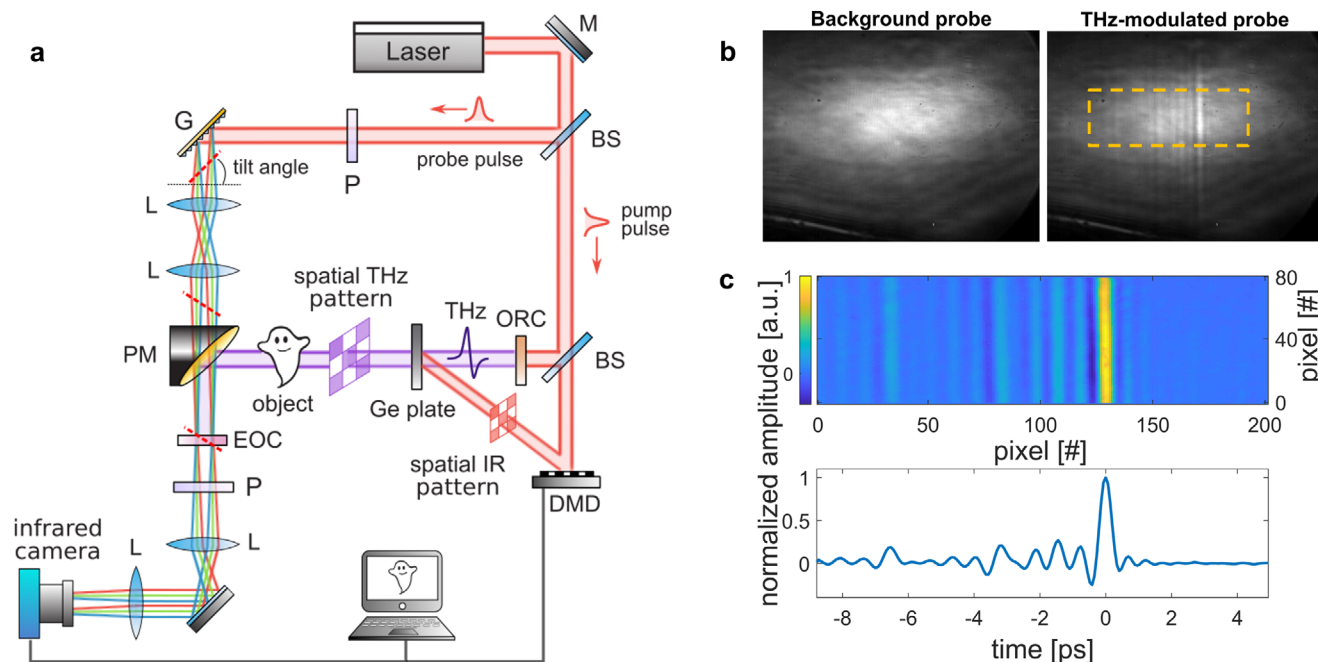


Figure 2. Operation of the THz scanless hypertemporal imaging system. a) Simplified diagram of the experimental setup. The laser beam is split into two lines (pump and probe) using a beam splitter (BS). The pump pulse is then split again: one line generates THz radiation via optical rectification in an organic crystal (ORC), the other is spatially modulated using a DMD; the patterned IR beam is used to photo-excite carriers in a Ge plate, in order to spatially modulate the THz pulse; the latter interrogates the sample and then reaches the detection crystal (EOC). The probe line goes through a polarizer (P) and then hits a grating (G), which tilts the probe pulse front; two lenses (L) form a 4-f system that images the tilted probe beam onto the detection crystal (EOC). After such crystal, an analyzer and a second 4-f system re-image the THz-modulated probe beam onto the IR camera. b) Examples of images recorded by the IR camera: background probe beam (left); THz-modulated probe beam (right). The dotted region corresponds to the area in (c). c) (Top) Portion of the area extracted from the images recorded by the camera and corrected by subtracting and dividing the modulated probe by the background; (bottom) THz waveform reconstructed by integrating the image above along the vertical direction.

32×32 frames for each sample, retrieved by taking, at every pixel, the normalized field amplitude at the time positions of the three THz amplitude peaks displayed in Figure 3e,f. Each image shows the spatial features of the layer with a thickness corresponding to that particular time delay (see also the full time-domain video in Supporting Information). The in-plane resolution is dictated by the pixel size utilized to generate the modulation patterns ($312.5 \mu\text{m}$ in this case). We can see that the reconstruction reproduces well the object shape, excluding some portions at the letter and sample edges, as well as some smaller features, where probably scattering effects play a role in reducing transmission.

2.3. THz Time-of-Flight Images

For the same samples, we also measured the time delay (peak-to-peak time distance) between a reference THz pulse propagating in air and the THz pulses retrieved at each pixel. We, therefore, obtained images where the pixel color displays the time delay experienced by the THz pulse at that position. By considering the HDPE group refractive index, we also extracted the relative thickness of the different layers. In Figure 4, we present both 16×16 and 32×32 images for the two samples. The time-of-flight reconstruction of 16×16 images is accurate and allows discerning the letters at each layer, although the limited resolution ($625 \mu\text{m}$) hinders the precise reconstruction of the smallest features. In the

32×32 images, the increased resolution clearly enables to better show the sharp spatial features. However, we also note that some pixels, mostly at the edges of the letters and the sample, fail to represent the proper time delay, most likely due to scattering as well as diffraction effects. Indeed, the pixel size is in this case $312.5 \mu\text{m}$, thus comparable to the central wavelength ($300 \mu\text{m}$ at 1 THz) of the THz pulses. This means that even after very short distances, the propagating beam will undergo diffraction modifications (Rayleigh range $\approx 0.3 \text{ mm}$ at 1 THz), which alter the pattern spatial distribution interrogating the sample, in turn leading to a potential reduction of the resolution of the reconstructed image. Here, the choice of the maximum number of pixels to be employed is thus a trade-off between the smallest spatial feature of the object to be resolved and the limitations imposed by diffraction. Even though diffraction of the patterns could be numerically corrected by means of post-processing techniques,^[48] in our investigation, for simplicity, we have limited such effect by using a thin Ge plate ($125 \mu\text{m}$) and by placing the sample directly after it.

2.4. Compressed Sensing Applied to Scanless THz Imaging

As a proof-of-principle, we also implemented a standard non-iterative CS algorithm^[49] to reconstruct the image using a number of patterns that is smaller than the total number of pixels

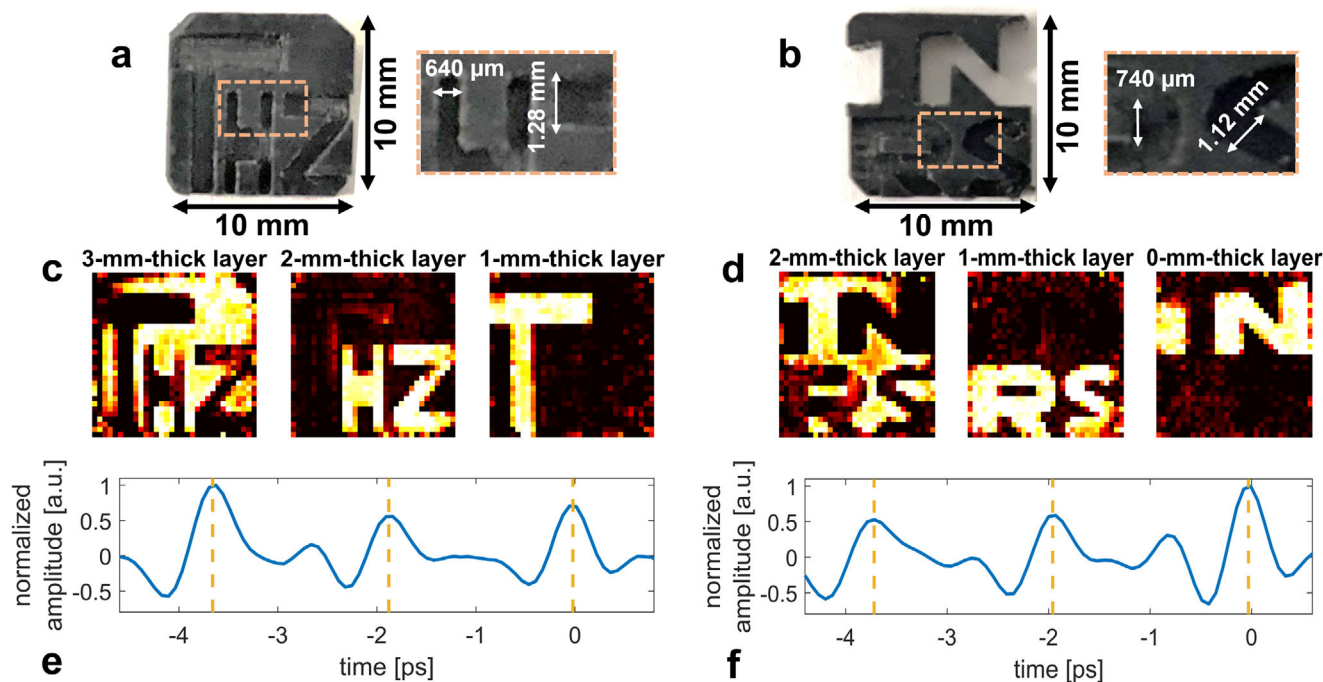


Figure 3. Image reconstruction. a) Sample (1), HDPE with T-H-Z letters engraved. b) Sample (2), HDPE with I-N-R-S letters engraved. c,d) Images reconstructed considering the electric field amplitude at the time positions corresponding to the three different peaks of the THz waveforms in (e,f) respectively. The waveforms in (e,f) are examples of measured THz traces before the SPI reconstruction is applied. The multipulse nature of these waveforms is due to the combined contributions from all the “white” pixels of the utilized pattern.

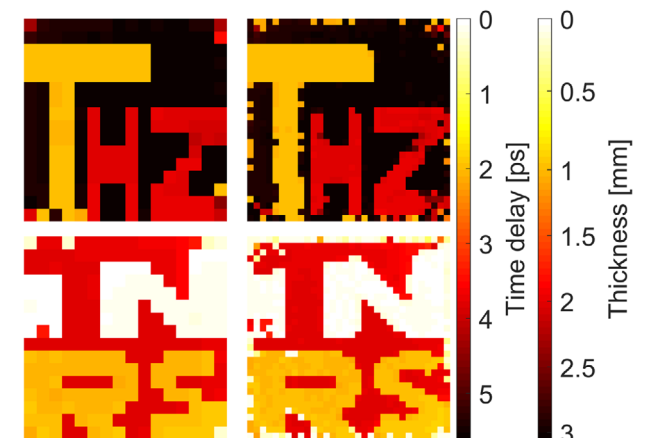


Figure 4. Time-delay images. (Top) Images of sample (1): (left) 16×16 and (right) 32×32 pixels images reconstructed considering the time delay between the THz pulse peak in air and the peak of the transmitted pulses retrieved at each pixel position. (Bottom) Images of sample (2): (left) 16×16 and (right) 32×32 pixels images reconstructed in the same way. The two color bars represent the temporal delay (left) and the local thickness of the samples (right).

(1024 in the case considered here). As shown in **Figure 5**, even using only 25% of the patterns (compression ratio, CR = number of patterns used/number of pixels), it is still possible to retrieve a good approximation of the spatial features of the three layers. Better compressions could be in principle achieved by using different pattern sets^[50] or more advanced reconstruction

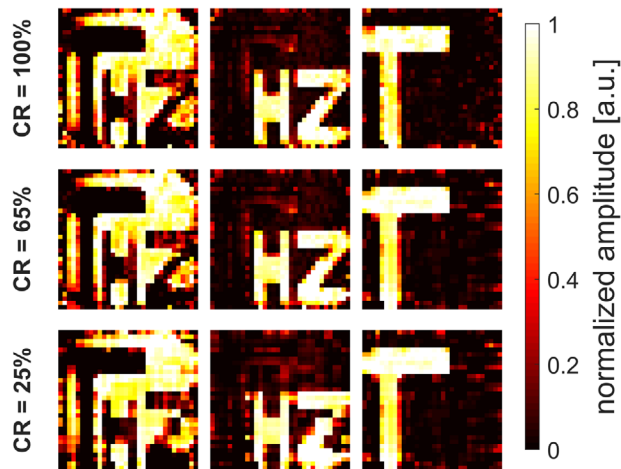


Figure 5. Compressed sensing reconstruction. 32×32 images of sample (1) reconstructed considering the amplitude at different time positions (as in Figure 3) and with a decreasing CR (from top to bottom, 100–65–25%).

algorithms.^[49] These solutions have been proven to be effective at optical frequencies but are not always straightforward to implement in the THz range, due to the limitations posed by the photo-modulation technique (for instance, the complexity in generating non-binary patterns). Innovative methods for THz modulation, potentially more flexible, have been introduced in recent years,^[31,51] but still need further development to become viable solutions.

3. Discussion and Conclusion

It is important to underline that, in the imaging examples shown above, from the same time-domain data we alternatively extracted the local transmitted amplitude as well as the delay relative to a reference pulse, thus making use of both amplitude and phase information. This is a demonstration that our imaging system fully preserves the capabilities of TDS coherent detection: depending on the type of sample under investigation, different contrast methods can thus be selected, so combining spatial 2D reconstruction with the extraction of, for example, the complex refractive index, time-of-flight information or even spectral absorption lines.^[34] At the same time, our arrangement is cost-effective and extremely simple, basically requiring, besides the laser source, just a DMD and a camera to operate, without the presence of any complex device (mechanical or not) needed to perform the spatial/temporal scans. The few components involved and the absence of any mechanical moving part could make our scheme promptly appealing for the realization of compact tabletop THz imaging devices, which could be used, for example, to perform fast non-destructive imaging of multilayered^[3] and biological samples,^[52] to quickly monitor food quality in industry,^[53] or for the in situ investigation of cultural heritage.^[54]

The acquisition of a 32×32 image (1024 patterns) using our current system still requires a long time (≈ 40 min.), mainly due to the need for a long average (2.5 s) for each frame captured by the camera in correspondence with each pattern (we note that the acquisition of the same image without the single-shot technique would take ≈ 40 h via our setup and a traditional delay line). Such time-consuming acquisition is necessary to obtain a sufficient SNR (≈ 150 in our experiments, defined as the peak THz field of the measured waveforms divided by the standard deviation of the noise floor) at the limited repetition rate of our THz source (250 Hz). The use of higher-repetition-rate sources for THz single-shot detection was explored by Z. Jiang and coworkers,^[55] who successfully employed an amplified laser delivering μJ -level pulses at 250 kHz to retrieve THz waveforms via a scanless technique. This result indicates that our imaging scheme could also be implemented using higher-repetition-rate lasers, thus potentially reducing the acquisition time of the whole hypertextemporal image to a few seconds. Moreover, as shown above, the application of CS algorithms could further speed up the image acquisition, by limiting the number of patterns to a small fraction of the full set, toward real-time operation.

In conclusion, we have presented a novel configuration for THz multidimensional imaging that combines the SPI scheme with a scanless time-domain detection technique, so to achieve fast imaging without the need for complex electronics and any bulky mechanical moving part. From a more fundamental viewpoint, we have shown that diffraction plays a crucial role in the proposed technique. In particular, the scanless single-point THz coherent detection implemented in this work counter-intuitively exploits time-to-space mapping at the detection plane to fully retrieve multidimensional images (time/frequency, in addition to space), with the further possibility of extending the technique to complex-valued patterns and objects without significant limitations. We envision that coupling our scheme to suitable high-repetition rate laser sources, such as those based on ytterbium-

doped fibers, could lead to compact THz hypertextemporal imagers operating in real time.

4. Experimental Section

Hadamard Pattern Set and “Cake-Cutting” Ordering: The choice of the set of patterns typically depends on the operating conditions (e.g., light source wavelength, resolution, source brightness). One of the most used pattern bases is the Hadamard set, which guarantees an optimal SNR.^[56] The Hadamard set is orthonormal and can be obtained with an iterative procedure.^[57] In the present work, its construction was achieved by means of a built-in Matlab function. To implement a fast compressed sensing reconstruction, the Hadamard set ordered in a “cake-cutting” sequence was used.^[57] This ordering ensured that the most significant patterns were always displayed first, leading to a better reconstruction with lower sampling ratios and at a lower computational cost.

Time-to-Space Encoding and Near-Zero Transmission Detection: The time-to-space scanless technique employed in this work is based on tilting the probe pulse front in such a way that spatially separated points arrive at the detection crystal at different times, therefore probing different temporal positions of the THz waveform simultaneously. The pulse front tilt is typically achieved by means of a dispersive element (e.g., transmission/reflection grating), which spatially separates different frequency components of the broadband probe pulse, and a 4- f system enabling the formation of an image of the (tilted) probe front at the detection crystal position. The resulting time window, τ , is a function of the probe beam diameter, σ , at the detection position, and the tilt angle, γ . The tilt angle can, in turn, be written in terms of the mean wavelength of the light used, $\bar{\lambda}$, the grating parameter, d , the magnification of the 4- f system, M , and the diffraction angle after the grating, β (c is the speed of light in vacuum):^[58]

$$\tau = \frac{\sigma \tan \gamma}{c} = \frac{\bar{\lambda} \sigma}{c M d \cos \beta} \quad (2)$$

In the next paragraph, quantitative estimations for our experimental conditions are presented. The detection of the THz pulses was performed in a near-zero transmission configuration.^[59] In more detail, a linear polarizer was placed after the detection crystal with its axis almost perpendicular to the input probe polarization direction, leading to a probe transmission close to zero. When the THz pulse was present, an electric-field-induced birefringence in the crystal (Pockels effect) changed the probe polarization state, thus modifying the intensity transmitted through the polarizer. In the single-shot setup, different points along the probe pulse front undergo a different polarization modification, corresponding to a different temporal position along the THz waveform. The probe beam was then imaged onto the camera and its intensity variations revealed the THz waveform temporal shape. The waveform was extracted by first subtracting the image of the background probe from the one modulated by the THz, and then dividing the result by the background, to correct for the Gaussian shape of the probe beam:

$$\Gamma = \frac{I_{\text{THz}} - I_{\text{bg}}}{I_{\text{bg}}} \quad (3)$$

Imaging Setup Details: The output from a solid-state amplified Yb laser (1030 nm, 175 fs pulse duration, 1 m) at 250 Hz repetition rate) was split into a pump beam, a probe beam, and a pattern generator by means of a 4:96 wedge window and a 50:50 beam splitter. The pump beam was used to produce THz pulses via optical rectification in a 300- μm -thick HMQ-TMS (2-(4-hydroxy-3-methoxystyryl)-1-methylquinolinium 2,4,6-trimethylbenzenesulfonate) organic crystal. After some magnifying optical elements, the THz beam propagated through a 125- μm -thick Ge plate (undoped, resistivity $> 40 \Omega\text{cm}$) used for spatial modulation, and eventually passed through the sample. The imaging area was $10 \times 10 \text{ mm}^2$, while the THz beam diameter was set to $\approx 18 \text{ mm}$ ($1/e^2$), to ensure a reasonably uniform illumination of the scene. Finally, free-space

electro-optic sampling was carried out via a 3-mm-thick gallium phosphide crystal, where the THz and probe beams were spatially overlapped. The SPI scheme requires spatial patterns to interrogate the sample. To obtain such patterns on the THz beam, a modulation technique based on carriers' photo-excitation in a semiconductor was applied, first described in ref. [30]. The required IR pattern generation beam was modulated by means of a DMD (LightCrafter4500, Texas Instruments) and illuminated the surface of the Ge plate, locally exciting photo-carriers. The THz pulse passing through the plate shortly after the excitation was screened where carriers were present, but transmitted (albeit partially reflected) elsewhere. By applying this technique, a modulation depth of about 90% (peak amplitude of the THz pulse) was achieved. To implement the scanless (single-shot) detection scheme described above, a reflection grating (1200 grooves per mm) was placed along the probe beam path, followed by a 4-f system (50 cm and 10 cm focal lengths), which imaged the probe onto the detection crystal with a reduced size (1 mm diameter) and a tilted front. After sampling the THz pulse, the probe was magnified by a second 4-f system (5 cm and 50 cm focal lengths) and then reached the recording IR camera (Xeva 320 Series, Xenics). With the grating employed and operating at an incidence angle of 72° (diffracted angle 16°), the expected available time window provided by the probe was $\tau \approx 19$ ps, which was suitable to properly acquire the THz waveforms replicas transmitted through the multilayered samples. The scanless detection was time calibrated by means of a mechanical delay line, by changing the probe optical path and checking the corresponding shift of the spatial position of the THz pulse peak on the camera. The temporal resolution obtained in our experimental conditions was 68.7 fs per pixel.

Supporting Information

Supporting Information is available from the Wiley Online Library or from the author.

Conflict of Interest

The authors declare no conflict of interest.

Data Availability Statement

The data that support the findings of this study are available from the corresponding authors upon reasonable request.

Keywords

compressed sensing, scanless acquisition, terahertz multidimensional imaging

Received: December 2, 2022
Revised: April 24, 2023
Published online: June 22, 2023

- [1] D. M. Mittleman, R. H. Jacobsen, M. C. Nuss, *IEEE J. Sel. Top. Quantum Electron.* **1996**, *2*, 679.
- [2] I. Duling, D. Zimdars, *Nat. Photonics* **2009**, *3*, 630.
- [3] A. Redo-Sanchez, B. Heshmat, A. Aghasi, S. Naqvi, M. Zhang, J. Romberg, R. Raskar, *Nat. Commun.* **2016**, *7*, 12665.
- [4] P. U. Jepsen, D. G. Cooke, M. Koch, *Laser Photonics Rev.* **2011**, *5*, 124.
- [5] J. Dai, J. Zhang, W. Zhang, D. Grischkowsky, *J. Opt. Soc. Am. B* **2004**, *21*, 1379.
- [6] R. H. Jacobsen, D. M. Mittleman, M. C. Nuss, *Opt. Lett.* **1996**, *21*, 2011.
- [7] B. N. Flanders, R. A. Cheville, D. Grischkowsky, N. F. Scherer, *J. Phys. Chem.* **1996**, *100*, 11824.
- [8] E. P. J. Parrott, J. A. Zeidler, *Appl. Spectrosc.* **2015**, *69*, 1.
- [9] G. Gallot, J. Zhang, R. W. McGowan, T. I. Jeon, D. Grischkowsky, *Appl. Phys. Lett.* **1999**, *74*, 3450.
- [10] G. Acbas, K. A. Niessen, E. H. Snell, A. G. Markelz, *Nat. Commun.* **2014**, *5*, 3076.
- [11] T. L. Cocker, D. Peller, P. Yu, J. Repp, R. Huber, *Nature* **2016**, *539*, 263.
- [12] T. Kampfrath, A. Sell, G. Klatt, A. Pashkin, S. Mährlein, T. Dekorsy, M. Wolf, M. Fiebig, A. Leitenstorfer, R. Huber, *Nat. Photonics* **2011**, *5*, 31.
- [13] B. B. Hu, M. C. Nuss, *Opt. Lett.* **1995**, *20*, 1716.
- [14] Y. C. Shen, T. Lo, P. F. Taday, B. E. Cole, W. R. Tribe, M. C. Kemp, *Appl. Phys. Lett.* **2005**, *86*, 241116.
- [15] C. Jördens, M. Koch, *Opt. Eng.* **2008**, *47*, 037003.
- [16] R. Naccache, A. Mazhorova, M. Clerici, R. Piccoli, L. K. Khorashad, A. O. Govorov, L. Razzari, F. Vetrone, R. Morandotti, *Laser Photonics Rev.* **2017**, *11*, 1600342.
- [17] A. G. Markelz, D. M. Mittleman, *ACS Photonics* **2022**, *9*, 1117.
- [18] E. Abraham, A. Younus, J. C. Delagnes, P. Mounaix, *Appl. Phys. A* **2010**, *100*, 585.
- [19] J. Dong, A. Locquet, M. Melis, D. S. Citrin, *Sci. Rep.* **2017**, *7*, 15098.
- [20] M. van Exter, D. R. Grischkowsky, *IEEE Trans. Microwave Theory Tech.* **1990**, *38*, 1684.
- [21] Q. Wu, X. C. Zhang, *Appl. Phys. Lett.* **1995**, *67*, 3523.
- [22] J. Dai, J. Liu, X. C. Zhang, *IEEE J. Sel. Top. Quantum Electron.* **2011**, *17*, 183.
- [23] H. Guerboukha, K. Nallappan, M. Skorobogatiy, *Adv. Opt. Photonics* **2018**, *10*, 843.
- [24] P. Sen, B. Chen, G. Garg, S. R. Marschner, M. Horowitz, M. Levoy, H. P. A. Lensch, in *ACM SIGGRAPH 2005 Papers on - SIGGRAPH '05*, Association for Computing Machinery, New York **2005**, p. 745.
- [25] M. F. Duarte, M. A. Davenport, D. Takbar, J. N. Laska, T. Sun, K. F. Kelly, R. G. Baraniuk, *IEEE Signal Process. Mag.* **2008**, *25*, 83.
- [26] E. J. Candes, M. B. Wakin, *IEEE Signal Process. Mag.* **2008**, *25*, 21.
- [27] M. P. Edgar, G. M. Gibson, M. J. Padgett, *Nat. Photonics* **2019**, *13*, 13.
- [28] W. L. Chan, K. Charan, D. Takhar, K. F. Kelly, R. G. Baraniuk, D. M. Mittleman, *Appl. Phys. Lett.* **2008**, *93*, 121105.
- [29] H. Shen, L. Gan, N. Newman, Y. Dong, C. Li, Y. Huang, Y. C. Shen, *Opt. Lett.* **2012**, *37*, 46.
- [30] D. Shrekenhamer, C. M. Watts, W. J. Padilla, *Opt. Express* **2013**, *21*, 12507.
- [31] C. M. Watts, D. Shrekenhamer, J. Montoya, G. Lipworth, J. Hunt, T. Sleasman, S. Krishna, D. R. Smith, W. J. Padilla, *Nat. Photonics* **2014**, *8*, 605.
- [32] Y. C. Shen, L. Gan, M. Stringer, A. Burnett, K. Tych, H. Shen, J. E. Cunningham, E. P. J. Parrott, J. A. Zeidler, L. F. Gladden, E. H. Linfield, A. G. Davies, *Appl. Phys. Lett.* **2009**, *95*, 231112.
- [33] R. I. Stantchev, D. B. Phillips, P. Hobson, S. M. Hornett, M. J. Padgett, E. Hendry, *Optica* **2017**, *4*, 989.
- [34] L. Zanutto, R. Piccoli, J. Dong, D. Caraffini, R. Morandotti, L. Razzari, *Opt. Express* **2020**, *28*, 3795.
- [35] L. Zanutto, R. Piccoli, J. L. Dong, R. Morandotti, L. Razzari, *Opto-Electron. Adv.* **2020**, *3*, 20001201.
- [36] J. W. Goodman, *Introduction to Fourier Optics*, 2nd ed., The McGraw-Hill Companies, **1996**.
- [37] R. Horisaki, H. Matsui, R. Egami, J. Tanida, *Appl. Opt.* **2017**, *56*, 1353.
- [38] M. Li, L. Bian, G. Zheng, A. Maiden, Y. Liu, Y. Li, J. Suo, Q. Dai, J. Zhang, *Opt. Lett.* **2021**, *46*, 1624.
- [39] P. Clemente, V. Durán, E. Tajahuerce, V. Torres-Company, J. Lancis, *Phys. Rev. A: At., Mol., Opt. Phys.* **2012**, *86*, 041803.
- [40] R. I. Stantchev, X. Yu, T. Blu, E. Pickwell-MacPherson, *Nat. Commun.* **2020**, *11*, 2535.

- [41] T. Yasui, E. Saneyoshi, T. Araki, *Appl. Phys. Lett.* **2005**, *87*, 061101.
- [42] B. Urbanek, M. Möller, M. Eisele, S. Baierl, D. Kaplan, C. Lange, R. Huber, *Appl. Phys. Lett.* **2016**, *108*, 121101.
- [43] S. M. Teo, B. K. Ofori-Okai, C. A. Werley, K. A. Nelson, *Rev. Sci. Instrum.* **2015**, *86*, 051301.
- [44] Y. Kawada, T. Yasuda, A. Nakanishi, K. Akiyama, H. Takahashi, *Opt. Express* **2011**, *19*, 11228.
- [45] D. J. Zhang, R. Yin, T. B. Wang, Q. H. Liao, H. G. Li, Q. Liao, J. T. Liu, *Opt. Commun.* **2018**, *412*, 146.
- [46] F. G. Sun, Z. Jiang, X. C. Zhang, *Appl. Phys. Lett.* **1998**, *73*, 2233.
- [47] M. Naftaly, R. E. Miles, *Proc. IEEE* **2007**, *95*, 1658.
- [48] Y. Shang, X. Wang, W. Sun, P. Han, J. Ye, S. Feng, Y. Zhang, *Opt. Express* **2019**, *27*, 14725.
- [49] L. Bian, J. Suo, Q. Dai, F. Chen, *J. Opt. Soc. Am. A* **2018**, *35*, 78.
- [50] Z. Zhang, X. Wang, G. Zheng, J. Zhong, *Opt. Express* **2017**, *25*, 19619.
- [51] W. Li, X. Hu, J. Wu, K. Fan, B. Chen, C. Zhang, W. Hu, X. Cao, B. Jin, Y. Lu, J. Chen, P. Wu, *Light: Sci. Appl.* **2022**, *11*, 191.
- [52] R. I. Stantchev, J. C. Mansfield, R. S. Edginton, P. Hobson, F. Palombo, E. Hendry, *Sci. Rep.* **2018**, *8*, 6924.
- [53] G. Ok, K. Park, H. J. Kim, H. S. Chun, S.-W. Choi, *Appl. Opt.* **2014**, *53*, 1406.
- [54] K. Krügener, M. Schwerdtfeger, S. F. Busch, A. Soltani, E. Castro-Camus, M. Koch, W. Viöl, *Sci. Rep.* **2015**, *5*, 14842.
- [55] Z. Jiang, X. C. Zhang, *Appl. Phys. Lett.* **1998**, *72*, 1945.
- [56] M. Harwit, N. J. A. Sloan, *Hadamard Transform Optics*, 1st ed., Academic Press, San Diego, CA **1979**.
- [57] W.-K. Yu, *Sensors* **2019**, *19*, 4122.
- [58] Y. Kawada, T. Yasuda, H. Takahashi, S. Aoshima, *Opt. Lett.* **2008**, *33*, 180.
- [59] Z. Jiang, F. G. Sun, Q. Chen, X. C. Zhang, *Appl. Phys. Lett.* **1999**, *74*, 1191.